Fundamental aspects of the structural and electrolyte properties of Li$_2$OHCl from simulations and experiment

Jason Howard,[1] Zachary D. Hood,[2,3] and N. A. W. Holzwarth[1,*]

[1]*Department of Physics, Wake Forest University, Winston-Salem, NC 27109-7507, USA*
[2]*Center for Nanophase Materials Sciences, Oak Ridge National Laboratory, Oak Ridge, TN 37831, USA*
[3]*School of Chemistry and Biochemistry, Georgia Institute of Technology, Atlanta, GA 30332, USA*

Solid-state electrolytes that are compatible with high-capacity electrodes are expected to enable the next generation of batteries. As a promising example, Li$_2$OHCl was reported to have good ionic conductivity and to be compatible with a lithium metal anode even at temperatures above 100 °C. In this work, we explore the fundamental properties of Li$_2$OHCl by comparing simulations and experiments. Using calculations based on density functional theory, including both static and dynamic contributions through the quasiharmonic approximation, we model a tetragonal ground state, which is not observed experimentally. An ordered orthorhombic low-temperature phase was also simulated, agreeing with experimental structural analysis of the pristine electrolyte at room temperature. In addition, comparison of the ordered structures with simulations of the disordered cubic phase provide insight into the mechanisms associated with the experimentally observed abrupt increase in ionic conductivity as the system changes from its ordered orthorhombic to its disordered cubic phase. A large Haven ratio for the disordered cubic phase is inferred from the computed tracer diffusion coefficient and measured ionic conductivity, suggesting highly correlated motions of the mobile Li ions in the cubic phase of Li$_2$OHCl. We find that the OH bond orientations participate in gating the Li ion motions which might partially explain the predicted Li-Li correlations.

I. INTRODUCTION

The drive to produce all-solid-state batteries has led to exploration of novel solid-state materials that can replace traditional liquid electrolytes. There are many factors that determine whether a material can be used in an electrochemical cell, with one of the most important being that it is a very good ionic conductor. With the demand for batteries to have large energy and volumetric densities, all solid-state lithium ion batteries are very promising. In a battery, the electrolyte functions to allow transport of the energy storing ion between the electrodes while preventing the passage of electrons. This allows for the electrons to be passed through an external circuit and do work. An efficient mechanism that often results in high mobility of the "working" ion involves lattice structures with fractionally occupied (disordered) sites for the working ion.

Recently, two independent experimental investigations [1,2] showed that introducing defects into the disordered phase of crystalline Li$_2$OHCl can enhance its Li ion conductivity, suggesting this system to be very promising as an electrolyte material for all solid-state Li ion batteries. Earlier studies reported that Li$_2$OHCl and related materials have a low-temperature orthorhombic structure [3,4] having low ionic conductivity and a high-temperature cubic structure [3–5] having increased ionic conductivity. The temperature of the phase transition has been reported [1,4] to be approximately 35 °C, depending upon sample preparation. In fact, very little is known about the low-temperature phase of Li$_2$OHCl other than its reported [3,4] orthorhombic structure. In this work, we report a detailed experimental and computational study of pure Li$_2$OHCl in both its low- and high-temperature structures

in order to understand their fundamental properties and their relationships to the electrolyte capabilities of this material.

II. METHODS

A. Computational methods

In this work, computations were based on density functional theory [6,7] using the projector augmented wave (PAW) formalism [8]. The ATOMPAW code [9] was used to generate the PAW basis and projector functions, and the solid-state materials were modeled with periodic boundary conditions using the QUANTUM ESPRESSO software package [10]. The software packages VESTA [11] and XCRYSDEN [12] were used for visualizations of structural properties at the atomic level, and FINDSYM [13] helped in space-group analysis of the structures. MATLAB [14] was used in the quasiharmonic analysis of the Helmholtz free energy on a three-dimensional grid of lattice parameters. It was also used in visualizing histograms of the OH orientations.

The exchange-correlation functional was approximated using the local-density approximation [15] (LDA). The choice of LDA functional was made based on previous investigations [16–18] of similar materials which showed that provided that the lattice constants are scaled by a correction factor of 1.02, the simulations are in good agreement with experiment, especially lattice vibrational frequencies and heats of formation.

In general, self-consistent field and structural optimization calculations were well converged with a plane-wave expansion of wave vectors and reciprocal lattice vectors including $|\mathbf{k} + \mathbf{G}|^2 \leqslant 64$ Ry. However, a larger plane-wave expansion including $|\mathbf{k} + \mathbf{G}|^2 \leqslant 90$ Ry was needed for using density functional perturbation theory, which involves evaluating derivatives with respect to atomic displacements [19–21],

---

*natalie@wfu.edu

for the simulations of the phonon modes, as discussed in Sec. III A 2. For converging the electronic structures of the tetragonal and orthorhombic structures, zone-centered **k**-point grids of $12 \times 12 \times 12$ and $12 \times 12 \times 6$ were used, respectively. The total energy tolerance of the self-consistent field calculations was set to 10^{-12} Ry and the resulting forces were converged within 7×10^{-4} eV/Å. The phonon density of states was calculated with an energy convergence parameter of 10^{-14} Ry for the density functional perturbation self-consistent cycles. The interatomic force constants were calculated from density functional perturbation theory using $3 \times 3 \times 3$ and $3 \times 3 \times 2$ zone-centered phonon **q**-point grids for the tetragonal and octahedral structures, respectively. The resultant force constants were then interpolated to evaluate the phonon density of states using the finer **q**-point mesh of $10 \times 10 \times 10$ and $10 \times 10 \times 5$ for the tetragonal and orthorhombic structures, respectively. The acoustic sum rule was imposed along the diagonal elements of the dynamical matrices [21] at $q = 0$.

In order to simulate the disordered cubic structures, the numerical accuracy of the calculations could be relaxed while ensuring that energy differences were calculated with errors less than 7×10^{-4} eV/formula-unit. The plane-wave expansion included $|\mathbf{k} + \mathbf{G}|^2 \leqslant 45$ Ry and the energy tolerance of the self-consistent field was set to 10^{-8} Ry. For simulations based on supercell sizes $2 \times 2 \times 2$, $3 \times 3 \times 3$, $4 \times 4 \times 4$, and $5 \times 5 \times 5$, using the corresponding zone-centered **k**-point sampling grids of $3 \times 3 \times 3$, $2 \times 2 \times 2$, $1 \times 1 \times 1$, and $1 \times 1 \times 1$, respectively. The molecular dynamics simulations were performed using $3 \times 3 \times 3$ supercells using a single zone-centered **k** point to sample the Brillouin zone. A time step of 0.96 fs was used for all simulations. Each simulation was done using the microcanonical ensemble (NVE). The temperature was controlled by initializing the atoms of the relaxed supercell with Boltzmann distribution of velocities corresponding to twice the target temperature. We found that within the first 0.03 ps of the simulation run, the temperature typically dropped to approximately its target temperature. Simulations were carried out for 60–135 ps. Throughout the simulations, we found that the total energy remained constant except for a small drift per formula unit of 6×10^{-7} eV/fs and a corresponding positive drift in the simulation temperature.

B. Experimental methods

In previous work [1], the "fast-cooled" samples of Li_2OHCl were reported. In this work, we focus on "slow-cooled" samples in order to make it easier to compare with model calculations. The synthesis of slow-cooled Li_2OHCl was based on the methods previously reported [1]. All reagents were dried under vacuum at 90 °C for 4 h prior to use. LiOH (Sigma Aldrich, $\geqslant 98\%$) and LiCl (Sigma Aldrich, $\geqslant 99\%$) were mixed in a nickel crucible and sealed with a copper gasket in a bomb reactor inside of an argon-filled glove box. The reactor was heated to 350 °C for 24 h at a rate of 25 °C/h, then slowly cooled to 250 °C at 8 °C/h, maintained at 250 °C for 24 h, and then cooled to room temperature at 25 °C/h. The material was then hand ground with a mortar and pestle for 10 min and ball milled (8000M Spex Mixer Mill) using a mixture of 3 and 5 mm Y-ZrO$_2$ ball milling media in a 1:25

(solid electrolyte: media) mass ratio in a HDPE vial. Due to the sensitivity of Li_2OHCl to moist air, all processes were completed under argon.

Identification of the crystalline phase for Li_2OHCl was conducted on a PANalytical X'pert Pro Powder Diffractometer with CuK α radiation ($\lambda = 1.54056$ Å). Powder samples were dispersed on quartz slides and sealed with Kapton® films. High-temperature x-ray diffraction (XRD) scans were conducted with an Anton Paar XRK 900 Hot Stage which was heated to 200 °C at 2 °C/min; the temperature was maintained for 20 min prior to collecting crystallographic data. Rietveld refinements and analysis of crystallographic data were completed with HIGHSCORE PLUS, which is a software package provided through PANanalytical.

Slow-cooled Li_2OHCl was cold pressed at 300 MPa in an airtight cell designed by our group with Al/C blocking electrodes for all electrochemical impedance spectroscopy (EIS) measurements (Bio-Logic, VSP). EIS measurements were measured between 1 mHz and 1 MHz with an amplitude of 100.0 mV in a temperature-controlled chamber. For Arrhenius measurements, the temperature control chamber was ramped from 25 °C to 200 °C and allowed to equilibrate for 2 h before EIS measurements were collected.

III. CRYSTAL STRUCTURE

A. Low-temperature structures of Li$_2$OHCl

1. Static lattice simulations

By static lattice simulations we mean simulations performed by assuming that the atomic positions are time independent, with no effects of quantum lattice vibrations taken into account. These results are obtained by optimizing the total energy with respect to atomic positions and simulation cell parameters within self-consistent density functional calculations.

One goal of the simulations is to make accurate models of the available experimental results. Information about the low-temperature structure of Li_2OHCl from experimental evidence can be summarized as follows. Below temperatures of approximately 35 °C, Schwering *et al.* [4] reported the structure of Li_2OHCl to be orthorhombic. The analyzed lattice constants were given as $a = 3.8220(1)$ Å, $b = 7.9968(2)$ Å, and $c = 7.7394(2)$ Å, and the space group $Amm2$ (#38) [22] was suggested. While the fractional coordinates of the atoms were not reported, the experimental study of the phase transition indicated the low-temperature phase to be ordered. The x-ray diffraction pattern of samples of the low-temperature phase of "fast-cooled" samples were also recently reported by Hood *et al.* [1], and analogous results for "slow-cooled" samples are presented in this work.

From this evidence, we carried out a computational structure search to determine the ground-state structure of Li_2OHCl. Several candidate structures were optimized using the density functional theory methods described in Sec. II A. The candidate structures were based on ordered variations of the cubic structure found in the literature [3]. As a result of this computational search, we found the lowest-energy structure to have a tetragonal lattice characterized by the space group $P4mm$ (#99) as shown in Fig. 1(a). (For convenience
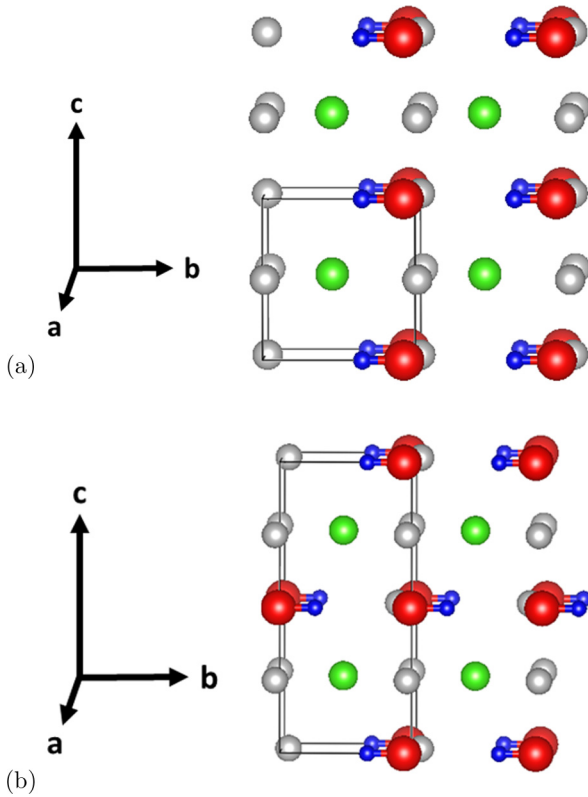
FIG. 1. Ball and stick representations of the computationally optimized structures of Li_2OHCl in the (a) tetragonal structure [space group $P4mm$ (#99), rotated by 90° about the a axis from the standard orientation] and (b) orthorhombic structure [space group $Pmc2_1$ (#26)]. For both structures, green balls represent Cl, red O, blue H, and silver Li.

in making structural comparisons, we rotated the standard lattice orientation by 90° about the a axis.) This ground-state structure has all of the OH groups oriented along the b axis and is very closely related to an ordered form of the high-temperature cubic structure which will be discussed in Sec. III B. The optimized lattice constants and fractional atomic coordinates are given in Table I.

The challenge introduced by this DFT ground-state structure is to reconcile the determined tetragonal structure with the experimental findings [1,4] of an orthorhombic structure. One variation of the ground-state structure that could give

TABLE I. DFT ground-state structure of Li_2OHCl having tetragonal structure with space group $P4mm$ (#99), using the nonstandard coordinates $x \rightarrow x$, $y \rightarrow z$, and $z \rightarrow -y$. The lattice constants (scaled by 1.02 to correct for the systematic LDA error) are $a = c = 3.794$ Å and $b = 3.578$ Å. The columns below list the atomic species, the multiplicity and Wyckoff label, and the fractional coordinates.

Atom	Wyckoff	x	y	z
O	1a	0.000	0.925	0.000
H	1a	0.000	0.654	0.000
Cl	1b	0.500	0.439	0.500
Li	2c	0.500	0.015	0.000

TABLE II. DFT metastable state structure of Li_2OHCl having orthorhombic structure with space group $Pmc2_1$ (#26). The lattice constants (scaled by 1.02 to correct for the systematic LDA error) are $a = 3.831$ Å, $b = 3.617$ Å, and $c = 7.985$ Å. The columns below list the atomic species, the multiplicity and Wyckoff label, and the fractional coordinates.

Atom	Wyckoff	x	y	z
O	2a	0.000	−0.024	0.000
H	2a	0.000	0.699	0.000
Cl	2b	0.500	0.500	0.250
Li	2a	0.000	0.001	0.250
Li	2b	0.500	0.086	0.000

rise to the orthorhombic structure is that the OH groups have a more complex orientational configuration compared with uniform alignment along the b axis. A structure search found a candidate orthorhombic structure having a DFT energy of 0.02 eV/FU (eV per formula unit) higher than the ground-state structure. Other distinct candidate orthorhombic structures were less stable by at least 0.1 eV/FU. This orthorhombic structure was found by optimizing the structure obtained by doubling the c axis of the tetragonal unit cell and coordinating the OH groups in opposite directions along the b axis. This structure has the space-group symmetry $Pmc2_1$ (#26). A visualization of this structure is shown in Fig. 1(b) and the lattice coordinates and fractional coordinates are given in Table II.

Although this candidate structure can explain the experimental observation of an orthorhombic unit cell, the computed lattice constants of $a = 3.831$ Å, $b = 3.617$ Å, and $c = 7.985$ Å (scaled by 1.02 to account for the systematic LDA error) are not in good agreement with the x-ray results measured in this work for the slow-cooled samples, nor the results reported by Schwering *et al.* [4], which correspond to $a = 3.8697$ Å, $b = 3.8220$ Å, and $c = 7.9968$ Å, presumably measured at room temperature. (Note that we assume that the mapping of the lattice convention used by Schwering *et al.* [4] to our convention corresponds to $a \rightarrow b$, $b \rightarrow c$, and $c/2 \rightarrow a$). Specifically, a significant discrepancy (of 5%) occurs for the optimized b-axis lattice constant. Similar difficulties in computing lattice constants associated with OH bonds using DFT-LDA for structural relaxation have been reported in the literature [23]. These observations motivated an extension of our simulations beyond the static lattice treatment.

2. Quasiharmonic simulations

The static lattice simulations described above are based on a purely classical treatment of the atomic nuclear positions. More realistically, the quantum mechanical physics of lattice vibrations can have significant effects on the structural properties of materials [24]. Within the context of a canonical ensemble, the appropriate thermodynamic energy is the Helmholtz free energy $F(T,a,b,c)$ as a function of temperature T and volume, which depends on the lattice parameters a, b, and c. (Note that in the present case, the experimental evidence suggests that it is sufficient to restrict consideration to orthorhombic structures, but in principle the

analysis could be extended to consider variations in the lattice angles α, β, and γ as well.) It is important to note that it is the Helmholtz free energy that is appropriate for this analysis (instead of the Gibbs free energy) because PV is small ($\sim 10^{-5}$ eV) at atmospheric pressures for these systems.

Within the Born-Oppenheimer approximation [25], the static lattice simulations well approximate the internal energy of the system due to the static nuclei and the corresponding total electronic energy $U_{SL}(a,b,c)$ for each set of lattice parameters a, b, and c. In principle, for each set of lattice parameters a, b, and c, the static lattice internal energy of a system can have a temperature dependence through its electronic degrees of freedom. However, for an ordered and electronically insulating material, it is reasonable to assume that the static lattice Helmholtz free energy is approximately temperature independent and dominated by the internal energy so that

$$F_{SL}(T,a,b,c) \approx U_{SL}(a,b,c). \quad (1)$$

Also within the framework of the Born-Oppenheimer approximation, the contributions of the lattice vibrations are energetically additive so that a reasonable approximation to the Helmholtz free energy can be determined from

$$F_{QH}(T,a,b,c) = U_{SL}(a,b,c) + F_{vib}(T,a,b,c), \quad (2)$$

where the subscript QH indicates the quasiharmonic approximation [21,26,27] and the vibrational Helmholtz free energy $F_{vib}(T,a,b,c)$ is evaluated at fixed lattice constants a,b,c using the harmonic approximation. Since we are examining ordered structures, it is not necessary to include effects of configurational entropy.

The quasiharmonic approximation [26] is based on the idea of calculating the vibrational Helmholtz free energy $F_{vib}(T,a,b,c)$ on a grid of lattice constants. For each set of lattice constants, the harmonic phonon spectrum is determined in terms of the phonon density of states $g(\omega,a,b,c)$:

$$g(\omega,a,b,c) = \frac{V}{(2\pi)^3} \int d^3q \sum_{\nu=1}^{3N} \delta(\omega - \omega_\nu(\mathbf{q},a,b,c)). \quad (3)$$

Here, V denotes the volume of the unit cell which contains N atoms. The integral over the phonon wave vectors $\mathbf{q}$ is taken over the Brillouin zone. For each $\mathbf{q}$, there are $3N$ normal mode frequencies ω_ν which contribute to the phonon density of states. These normal mode frequencies are determined from the eigenvalues of the dynamical matrix determined from the harmonic perturbations of the atomic positions $\tau_i(\mathbf{R}) = \tau_i^0 + \mathbf{R} + \mathbf{u}_i(\mathbf{R})$ for each atom i in each unit cell translated from the central cell by lattice translation $\mathbf{R}$. Here, τ_i^0 denotes the equilibrium position of the ith atom relative to the origin of the unit cell and $\mathbf{u}_i(\mathbf{R})$ denotes its harmonic displacement in cell $\mathbf{R}$.

Examples of the calculated phonon densities of states for two different sets of lattice constants a, b, and c are given in Fig. 2. The two sets of lattice constants were chosen as those that optimize the Helmholtz free energy at the temperature $T = 61$ and 301 K as will be explained later.
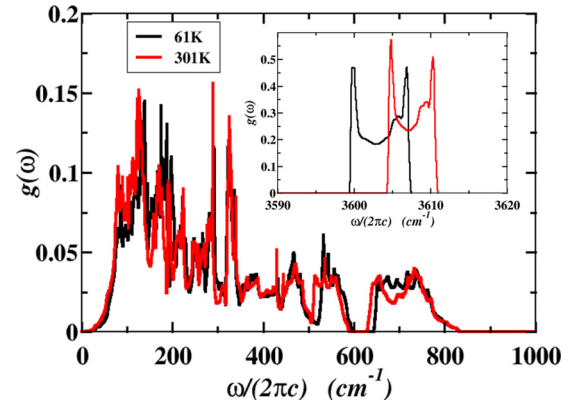

FIG. 2. Plots of $g(\omega,a,b,c)$ for two different sets of lattice parameters for the orthorhombic phase of Li_2OHCl. The sets of lattice parameters chosen for these plots correspond to optimal parameters found in this work. The inset shows the contributions to $g(\omega,a,b,c)$ from the high-frequency contributions on an expanded scale, corresponding to the stretching of the OH bonds.

For each set of lattice constants, a, b, and c, the static lattice internal energy corresponds to

$$U_{SL}(a,b,c) \equiv U_{SL}\big(a,b,c,\{\tau_i^0\}\big). \quad (4)$$

The Hessian matrix of the static lattice internal energy corresponds to the "analytic" part of the dynamical matrix expressed in terms of atoms i and j (with masses M_i and M_j) in the unit cell and displacement directions α and β [20,24]:

$$\tilde{D}_{i\alpha,j\beta}^{an}(\mathbf{q},a,b,c) = \frac{1}{\sqrt{M_i M_j}} \sum_{\mathbf{R}} e^{i\mathbf{q}\cdot\mathbf{R}} \frac{\partial^2 U_{SL}\big(a,b,c,\{\tau_i^0\}\big)}{\partial u_{i\alpha}(\mathbf{0})\partial u_{j\beta}(\mathbf{R})}. \quad (5)$$

Here, the summation over $\mathbf{R}$ represents the summation over all lattice translations. The evaluation of the Hessian includes both contributions from valence electron response and from the ions (nuclei and frozen core electrons) of the system evaluated within the QUANTUM ESPRESSO code [10]. For a phonon mode having wave vector $\mathbf{q}$, it can be assumed that the displacement can be expressed in terms of a complex amplitude vector according to

$$\mathbf{u}_i(\mathbf{R}) = \tilde{\mathbf{u}}_i(\mathbf{q})e^{i\mathbf{q}\cdot\mathbf{R}}. \quad (6)$$

In terms of these amplitudes, the valence electron response contributions are evaluated using density functional perturbation theory [19–21]. In ionic materials, such as in this study, the full dynamical matrix $\tilde{D}_{i\alpha,j\beta}(\mathbf{q},a,b,c)$ has an additional "nonanalytic" term representing coupling of the phonon modes near $\mathbf{q} \approx 0$ with an electromagnetic field [20,21], which is also evaluated in the QUANTUM ESPRESSO code [10]. Once the dynamical matrix is evaluated for each set of lattice parameters, it can be diagonalized to find the normal mode frequencies $\omega_\nu(\mathbf{q},a,b,c)$ and their corresponding amplitudes $A_{i\alpha}^\nu(\mathbf{q},a,b,c)$:

$$\sum_{j\beta} \tilde{D}_{i\alpha,j\beta}(\mathbf{q})A_{j\beta}^\nu(\mathbf{q},a,b,c) = \omega_\nu^2(\mathbf{q},a,b,c)A_{i\alpha}^\nu(\mathbf{q},a,b,c). \quad (7)$$

From the phonon density of states, the vibrational Helmholtz free energy is given by [24]

$$F_{\text{vib}}(T,a,b,c) = k_B T \int_0^\infty \ln\left[2\sinh\left(\frac{\hbar\omega}{2k_B T}\right)\right]$$
$$\times\, g(\omega,a,b,c)\, d\omega, \tag{8}$$

where k_B denotes the Boltzmann constant. In order to analyze the various contributions, the corresponding vibrational internal energy is given by

$$U_{\text{vib}}(T,a,b,c) = \frac{\hbar}{2} \int_0^\infty \omega \coth\left(\frac{\hbar\omega}{2k_B T}\right) g(\omega,a,b,c)\, d\omega, \tag{9}$$

and the vibrational entropy can be determined from

$$S_{\text{vib}}(T,a,b,c) = \frac{U_{\text{vib}}(T,a,b,c) - F_{\text{vib}}(T,a,b,c)}{T}. \tag{10}$$

At each temperature T it is possible to minimize the Helmholtz free energy to determine the optimal lattice parameters $a(T)$, $b(T)$, and $c(T)$ for each structure

$$F_{\text{min}}(T) = \min_{(a,b,c)} F_{\text{QH}}(T,a,b,c), \tag{11}$$

by interpolating the values of $F_{\text{QH}}(T,a,b,c)$ evaluated on the lattice constant grid.

In practice, for each system, the grid of lattice constants must be chosen to contain the minimum of the free energy. For analyzing the tetragonal structure of Li$_2$OHCl, a $4\times4\times4$ grid was chosen with a uniform grid spacing of approximately 0.095 Å. The range of lattice constants in Å units was $3.720 \leqslant a$ or $c \leqslant 4.006$, and $3.508 \leqslant b \leqslant 3.794$. For the orthorhombic structure of Li$_2$OHCl, a $5\times6\times5$ grid was chosen with a uniform grid spacing of approximately 0.073 Å. For this case, the range of lattice constants in Å units was $3.659 \leqslant a \leqslant 3.952$, $3.466 \leqslant b \leqslant 3.833$, and $7.725 \leqslant c \leqslant 8.017$. For each grid point of the lattice constants, the static lattice internal energy $U_{\text{SL}}(a,b,c)$ was determined by optimizing the internal atomic coordinates within the self-consistent density functional formalism. In order to ensure that the optimized structure corresponded to an equilibrium configuration, it was helpful to repeat the optimization with initial atomic coordinates differing slightly from the configurations shown in Fig. 1 with the use of random noise. It was found that for the orthorhombic structure, stable structures could be obtained by adding the noise only along the b axis. With this added precaution, it was possible to perform the harmonic phonon calculations at each grid point of the lattice constants without finding any imaginary (unstable) vibrational modes, indicating the validity of the quasiharmonic approximation for these systems and thus determining the phonon density of states $g(\omega,a,b,c)$.

The results of these calculations proved to be interesting in several aspects. First, in analyzing the optimized Helmholtz free energies per formula unit for the tetragonal phase and orthorhombic phase shown in Fig. 3, it is shown that the tetragonal phase is predicted to be thermodynamically favorable relative to the orthorhombic phase in the temperature range from 0 to 425 K. It is important to note the sensitivity to the crossing point of the free energies in Fig. 3 to a small
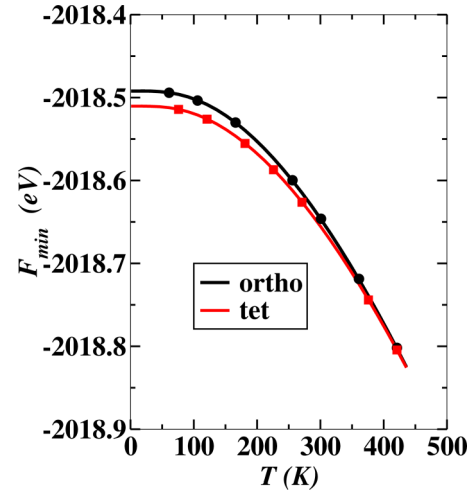

FIG. 3. Optimized Helmholtz free energy F_{min} (eV/FU) as a function of temperature T (K) computed for the tetragonal (red line) and orthorhombic (black line) structures of Li$_2$OHCl. The solid lines were determined by interpolation of the grid values, while the symbols represent values of $F_{\text{min}}(T)$ recalculated at the minimum lattice constants for the given temperature. The zero of energy (specifically for U_{SL}) is arbitrary but consistent throughout this paper.

error in the calculation. A relative error of ±0.01 eV shifts the crossing point of the relative free energies by $\sim\pm100$ K. While there is a large error bar on the transition temperature, the simulations suggest that the tetragonal phase should be thermodynamically stable at low temperatures. In fact, to the best of our knowledge, the tetragonal phase has not been reported in the experimental literature nor in the experimental x-ray analyses of this work. Since the tetragonal structure requires all of the OH groups to be aligned in the same direction, perhaps there are kinetic reasons which disfavor the tetragonal structure.

It is also interesting to look at the temperature dependence of the optimized lattice parameters $a(T)$, $b(T)$, and $c(T)$ for the tetragonal and orthorhombic phases as shown in Fig. 4. The lattice parameters for the tetragonal phase are continuous, and show a gentle increase in the lattice parameters across the temperature range. The lattice parameters for the orthorhombic phase are also continuous with a more rapid increase in $b(T)$ and smaller rapid decrease in $a(T)$ at T 150 K. Table III lists some typical values of the low-temperature and room-temperature optimized lattice parameters for both the tetragonal and orthorhombic phases. Comparing the low-temperature results computed within the quasiharmonic approximation with the corresponding static lattice results, we see that effects of lattice vibrations are to generally increase the lattice constants with largest increase occurring along the b axis which is the axis along which the OH bonds are aligned in these structures. The simulated lattice constants for the orthorhombic structure at room temperature in the quasiharmonic approximation are closer to the experimental results compared with the static lattice simulations.

To compare the theoretical x-ray diffraction with experiment, the atomic coordinates of orthorhombic structure were relaxed at the predicted room-temperature lattice constants; these atomic coordinates were used in a simulation cell with
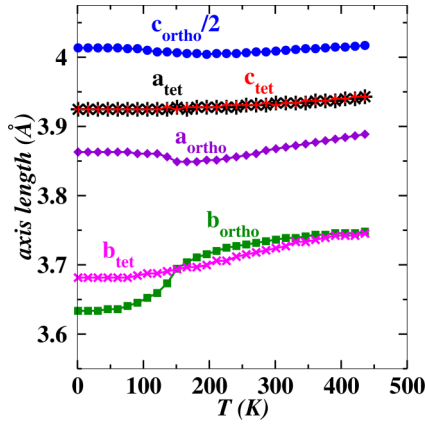
FIG. 4. Comparison of each of the lattice parameters as a function of temperature, calculated by optimizing $F_{min}(T)$ at each temperature and by multiplying by 1.02 to account for the systematic LDA error, comparing both the theoretical tetragonal and orthorhombic structures.

the theoretical corrected lattice parameters from Table III to produce theoretical x-ray diffraction patterns to compare with experiment. A comparison is shown in Fig. 5 with the orthorhombic structure before the quasiharmonic corrections, the room-temperature x-ray diffraction for the theoretical quasiharmonic corrected coordinates and lattice parameters from Table III, theoretical coordinates with experimental lattice parameters from Table III, and the experimental x-ray diffraction in this work. It is apparent that the x-ray diffraction for the theoretical atomic coordinates with experimental lattice parameters from this work is in good agreement with the experimental diffraction peaks measured in this work, while the purely theoretical quasiharmonic peaks are in reasonable agreement. It is noted that the quasiharmonic correction does improve the comparison with experiment. Its biggest effect is to increase the b lattice parameter by 0.1 Å relative to the static lattice value, while the experimental

TABLE III. Summary of low-temperature and room-temperature lattice parameters (in Å units) for Li_2OHCl calculated from the quasiharmonic approach defined in Eq. (11), scaled by a factor of 1.02 to account for the systematic LDA error. Results for both the tetragonal (tet) and orthorhombic (ortho) phases are tabulated at low temperature and at room temperature and compared with static lattice (SL) results. The simulation results are compared with experiment.

	a (Å)	b (Å)	c (Å)
tet SL	3.79	3.58	3.79
tet at $T = 106$ K	3.92	3.69	3.92
tet at $T = 271$ K	3.93	3.71	3.93
ortho SL	3.83	3.62	7.98
ortho at $T = 106$ K	3.86	3.65	8.02
ortho at $T = 271$ K	3.86	3.73	8.02
Experiment[a]	3.8697(1)	3.8220(1)	7.9968(2)
Experiment[b]	3.8749(8)	3.8257(8)	7.999(1)

[a]From Schwering in Ref. [4], mapping the reported values for the $c/2$, a, and b axes into the a, b, and c axes of this work.
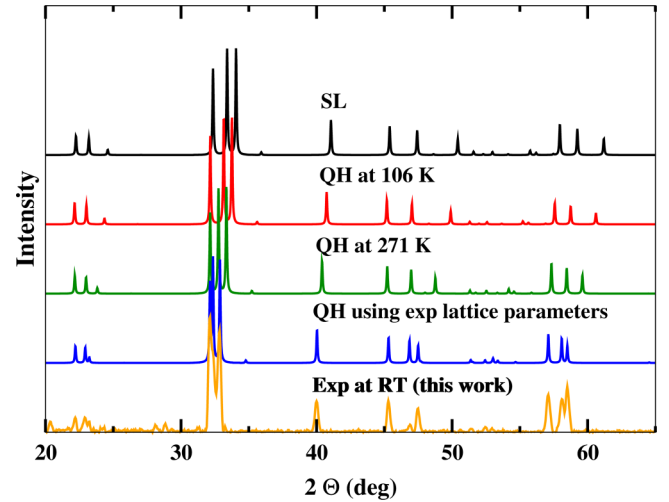[b]Measured in this work at $T = 294.25$ K.

FIG. 5. Comparison of simulated and experimental x-ray diffraction ($\lambda = 1.54056$ Å) patterns for the orthorhombic structure of Li_2OHCl. Black (top) shows the simulated result corresponding to the static lattice approximation. Red and green curves (upper middle) show the simulated result corresponding to the quasiharmonic approximation at 106 and 271 K, respectively. Blue curve (lower middle) was derived using the lattice parameters measured in this work and the fractional coordinates of the quasiharmonic simulations at 271 K. Orange (bottom) curve represents experimental measurements in this work.

b-axis lattice parameter is 0.2 Å larger than the static lattice value. The corresponding computed fractional coordinates for the orthorhombic structure were found to be insensitive to experiment, with the largest change occurring for the H site and for one of the Li sites which vary by approximately 0.01 fractional units along the b axis between $T = 106$ and 271 K.

In order to get more information about these results, it is helpful to look at separate contributions to the free energy. Figure 6 shows the static lattice internal energy $U_{SL}(a(T),b(T),c(T))$, the vibrational internal energy in the quasiharmonic approximation [according to Eq. (9)] $U_{vib}(T,a(T),b(T),c(T))$, and the vibrational entropy in the quasiharmonic approximation [according to Eq. (10)] $S_{vib}(T,a(T),b(T),c(T))$ [as represented by $-TS_{vib}(T,a(T),b(T),c(T))$, in parts (a), (b), and (c), respectively]. In comparing the internal energies U_{SL} and U_{vib} for the tetragonal and orthorhombic structures as a function of temperature, it is seen that both of these increase with increasing T. The static lattice internal energy $U_{SL}(a(T),b(T),c(T))$ differs for the two structures by 0.02 eV or more throughout the temperature range. The vibrational internal energy $U_{vib}(T,a(T),b(T),c(T))$ for the tetragonal structure is slightly larger than that of the orthorhombic structure by 0.005 eV or less throughout the temperature range. The difference in the vibrational entropies $S_{vib}(T,a(T),b(T),c(T))$ for the two structures becomes larger at higher temperatures, with the orthorhombic structure having higher entropy. The orthorhombic structure has a steeper rise in its static lattice internal energy but at higher temperatures, the larger entropy means that eventually the $-TS$ contribution of the phonon free energy lowers the total free energy of the orthorhombic structure below that of the tetragonal structure.
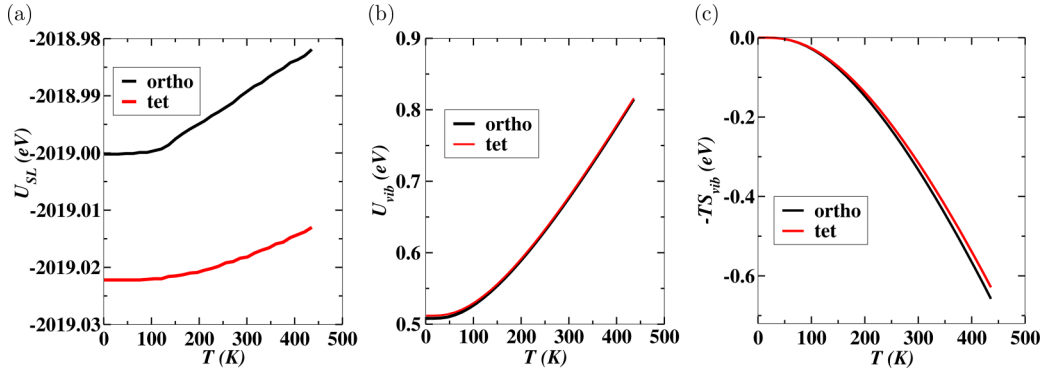
FIG. 6. Plots of thermodynamic quantities for the theoretical tetragonal and orthorhombic structures. Black is orthorhombic and red is tetragonal for all plots. Part (a) shows $U_{SL}(a(T),b(T),c(T))$ determined from the static lattice DFT total energies at the optimized lattice constants for temperature T. The zero of energy for U_{SL} is arbitrary, but consistent throughout this paper. (b) Shows the vibrational internal energy $U_{vib}(T,a(T),b(T),c(T))$. (c) Shows the vibrational entropy contribution in terms of $-T S_{vib}(T,a(T),b(T),c(T))$.

For example, our calculations find that at $T = 300$ K, $-T[S_{vib}(\text{ortho}) - S_{vib}(\text{tet})] = -0.02$ eV. The increase in entropy for the orthorhombic structure can be attributed to a shift in the phonon density of states to lower frequencies in the frequency range of $0 \leqslant \omega/(2\pi c) \leqslant 1000$ cm^{-1} as shown in Fig. 2.

Having found a reasonable model for the orthorhombic phase of Li$_2$OHCl, it is useful to focus on some of the details of the computational results for that system. One interesting feature of the computed orthorhombic phase is a predicted abrupt but continuous change of the b-axis parameter near $T = 150$ K as shown in Fig. 4. To investigate this further, contour plots of the free energy $F_{QH}(T,a,b,c)$, with the c axis

fixed at the predicted value for that temperature and in the entire plane of the interpolated results for the a and b axes, are presented in Fig. 7. The results show that going from low to high temperature, there is an expansion/elongation of the free energy minimum at the transition followed by a recentering and steepening of the minimum.

B. High-temperature structures of Li$_2$OHCl

The phase transition of Li$_2$OHCl has been observed [4] at temperatures above 35 °C, changing between the orthorhombic structure to cubic structure with heating. Hysteresis has been observed during the heating and cooling cycles. Evidence from
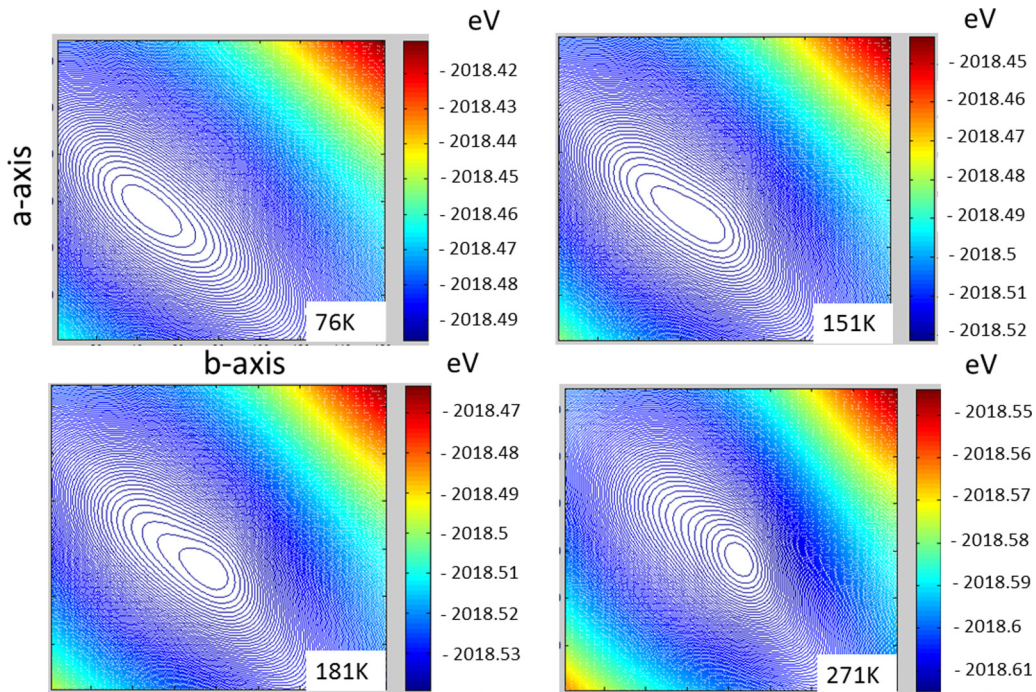

FIG. 7. Contour plots of the computed Helmholtz free energy $F(T,a,b,c(T))$ of the orthorhombic structure for four representative temperatures T. For each T, the plot spans the full grid of points in the a-b plane at the optimized value of $c(T)$. The vertical axis corresponds to the a axis which spans the range $3.659 \leqslant a \leqslant 3.952$ Å, the horizontal to the b axis which spans the range between $3.466 \leqslant b \leqslant 3.833$ Å.

TABLE IV. Fractional coordinates and site occupancies for the cubic $Pm\bar{3}m$ (#221) structure of Li_2OHCl. The columns below list the atomic species, the multiplicity and Wyckoff label, the fractional coordinates, and their occupancy factors as determined by Ref. [3]. The H coordinates were not determined.

Atom	Wyckoff	x	y	z	occ.
O	$1a$	0	0	0	1
Cl	$1b$	$\frac{1}{2}$	$\frac{1}{2}$	$\frac{1}{2}$	1
Li	$3d$	$\frac{1}{2}$	0	0	$\frac{2}{3}$

nuclear magnetic resonance (NMR) analysis [4] is consistent with the cubic structure being disordered as is consistent with the structure of the deuterated material, Li_2ODCl, which was analyzed by Eilbracht et al. [3] to have the space group $Pm\bar{3}m$ (#221). The corresponding atomic positions and their fractional occupancies are listed in Table IV. The lattice parameter of cubic Li_2OHCl was reported by Schwering et al. [4] to be $a = 3.9103(1)$ Å. A visualization of the unit cell indicating the fractional occupancy is shown in Fig. 8(a), while a model structure based on an optimized $5 \times 5 \times 5$ supercell is shown in Fig. 8(b).

In order to better understand the disordered system, several models were investigated. Supercells were prepared with lithium, oxygen, and chlorine at their ideal positions from Table IV, choosing two-thirds occupation of the lithium sites at random. The hydrogen sites were placed randomly on 4π

FIG. 8. (a) Shows a possible structure for a unit cell of cubic Li_2OHCl with shaded white and gray balls indicating the partially occupied Li sites. (b) Shows an optimized structure for a $5 \times 5 \times 5$ supercell of the disorder structure. The Li, O, H, and Cl sites are indicated with silver, red, blue, and green balls, respectively.

solid angles corresponding to the surfaces of spheres about each oxygen site having radii equal to 1 Å, representing the bond length of OH. These supercells were initialized at the cubic lattice parameters reported by Schwering et al. [4] and then all cell dimensions and atomic positions allowed to relax. This was done for 20 examples of $2 \times 2 \times 2$, 10 examples of $3 \times 3 \times 3$, 3 examples of $4 \times 4 \times 4$, and 2 examples of $5 \times 5 \times 5$ supercells. A visualization of one of the relaxed $5 \times 5 \times 5$ supercells is shown in Fig. 8(b). All of the relaxed configurations show deviation from cubic symmetry; one expects that a typical small piece of disordered material will produce a noncubic strain. In the limit of large bulk these strains should average out giving the cubic structure. The average of the axis lengths and axis angles for the progressively larger supercells is shown in Figs. 9(a) and 9(b), respectively, with error bars indicating the standard deviation (as distinct from the standard deviation of the mean). The results show that the standard deviation of the results gets smaller as the cell size increases; this is is indicative of the disordered model going to cubic in the large supercell limit. The average of the axes for the $5 \times 5 \times 5$ supercell calculations is taken as the estimate for the theoretical disordered cubic lattice parameter, which is 3.87 Å compared to the 3.91 Å reported by Schwering et al. [4].

As a further check on the simulated structure, the diffraction pattern for the the $5 \times 5 \times 5$ optimized supercell model shown Fig. 8(b) is compared with simulated x-ray pattern generated using the lattice parameters given by Schwering et al. [4] and with the experimental x-ray pattern measured in this work. Note that the lattice constant measured in this work is $a = 3.9083(1)$ Å at $T = 323.15$ K and $a = 3.9345(1)$ Å at $T = 473.15$ K which compares well with the value $a = 3.9103(1)$ Å reported by Schwering et al. [4]. The results are presented in Fig. 10. The agreement between the diffraction patterns is very good and shows that even with the large atomic relaxations relative to the ideal structure, the diffraction peaks are very sharp. In this case, the mobile species, Li^+ ions and H associated with OH groups, slightly perturb the less mobile diffracting species and have themselves very small diffraction cross sections.

IV. IONIC CONDUCTIVITY AND MOLECULAR DYNAMICS SIMULATIONS

The ionic conductivity versus temperature behavior of samples of Li_2OHCl for "slow-cooled" samples prepared in this study are presented as the red circles shown in Fig. 11. The results are similar to those presented in Ref. [1] for fast-cooled samples. The jump by more than a factor of 10 in the conductivity for temperatures near $T \approx 310$ K corresponds to the orthorhombic $\leftrightarrow$ cubic structural change. A similar but larger conductivity jump for samples of Li_2OHCl was reported by Schwering et al. [4].

Molecular dynamics simulations were carried out to better understand both the lithium ion diffusion and conductivity and the structural properties of the cubic phase of Li_2OHCl. The simulations were carried out for two unique starting configurations constructed as described in Sec. III B for $3 \times 3 \times 3$ supercells. For these simulations, the cubic lattice parameters were taken from the experimental parameters [4], reduced
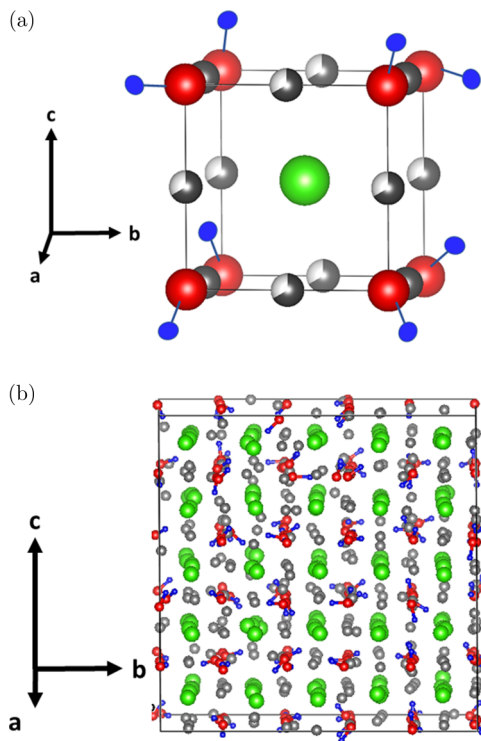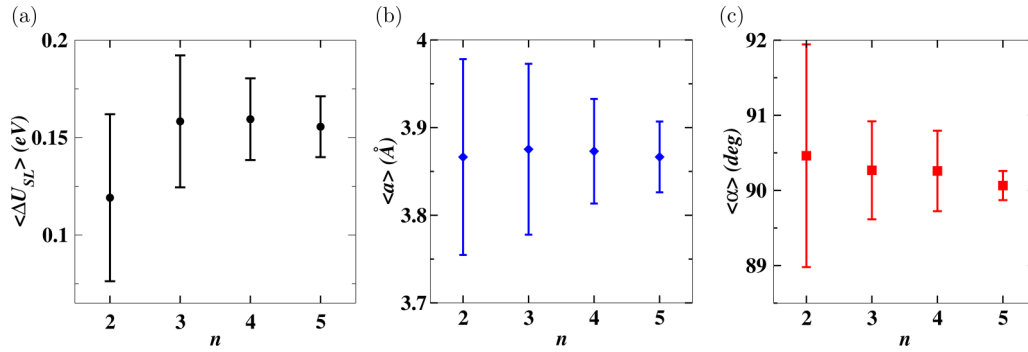
FIG. 9. Summary of results for optimized models of Li$_2$OHCl in its disordered cubic structures plotted as a function of n used to construct $n \times n \times n$ supercells in each case. The average value is indicated with a filled symbol and the error bars in the plots indicate the standard deviation. (a) $\langle \Delta U_{SL} \rangle$ denotes the average static lattice internal energy per cubic unit cell of the model configuration relative to the corresponding internal energy in the tetragonal phase. (b) $\langle a \rangle$ denotes the average cubic lattice parameter. (c) $\langle \alpha \rangle$ denotes the average lattice angle.

by 2% to approximate the LDA correction. The molecular dynamics simulations were carried out at constant volume in the manner described in the Methods section (Sec. II A) for the target temperatures in the range of $T = 300$–600 K which resulted in 14 molecular dynamics samples at computed temperatures in the range of $T = 350$–700 K. As discussed in further detail below, the simulations for one of the initial configurations configurations was carried out for approximately 120 ps, while the other configuration was carried out for approximately 60 ps. The similarity of analyzed results from the two initial configurations at equivalent temperatures suggest some degree of sampling convergence. Of course, it is always the case that the molecular dynamics results would benefit from longer simulation times. On the other hand, the analysis shows that during the simulation runs at even for the lowest-temperature simulations, 354 and 396 K, there are 5 and 17 hopping events, respectively. This indicates the presence of

low-energy activation barriers for hopping in this disordered system. These events were counted by assigning each Li to its nearest lattice site according to the simulation data of each run and then counting the number of discrete site transitions during the simulation.

Based on Kubo's analysis of the fluctuation-dissipation theorem in the context of evaluating transport properties of materials, the conductivity σ of a system is related to the averaged correlation function of current density $\mathbf{J}(t)$ of the system [28,29]

$$\sigma = \frac{V}{3k_B T} \int_0^\infty \langle \mathbf{J}(t) \cdot \mathbf{J}(0) \rangle dt. \tag{12}$$

In this expression, V represents the volume of the simulation cell, k_B is the Boltzmann constant, and T is the temperature. The angular brackets indicate ensemble averaging over initial configurations and the evaluation averages the diagonal of the conductivity tensor. For a system having ions of charge eQ_i
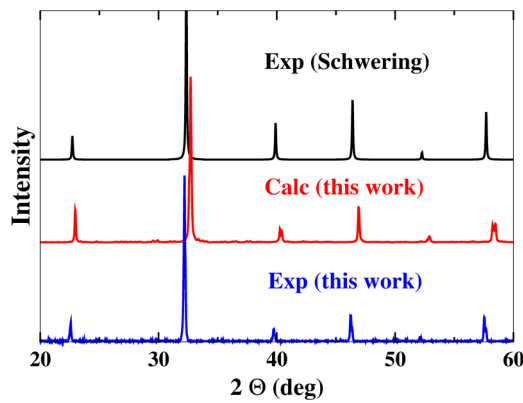

FIG. 10. X-ray diffraction ($\lambda = 1.54056$ Å) results of the cubic phase of Li$_2$OHCl, comparing simulated and measured intensities as a function of 2Θ (deg). The top plot was generated using the lattice parameters given by Schwering *et al.* [4] and fractional coordinates of the ideal disordered lattice. The second plot is the diffraction pattern generated from the $5 \times 5 \times 5$ optimized supercell model shown Fig. 8(b) and the bottom plot is an experimental x-ray pattern measured at $T = 323.15$ K for a slow-cooled sample synthesized in this work.
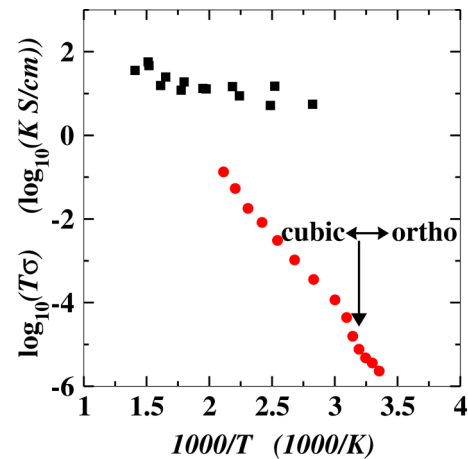

FIG. 11. Red circles correspond to the measured relationship between ionic conductivity σ (S/cm) and temperature T (in K) for slow-cooled samples of Li$_2$OHCl plotted as $\log_{10}(T\sigma)$ versus $1000/T$. The black squares correspond to the simulated conductivity inferred from tracer diffusion values according to Eq. (20) in terms of $\log_{10}(T\sigma H_r)$ versus $1000/T$.

and instantaneous particle velocities $\dot{\mathbf{R}}_i(t)$, the current density is given by

$$\mathbf{J}(t) = \frac{e}{V} \sum_{i=1}^{N} Q_i \dot{\mathbf{R}}_i(t), \qquad (13)$$

where the summation over particles i includes all N ions in the simulation cell. By integrating Eq. (12) over time, the conductivity can be expressed in terms of the instantaneous particle positions $\mathbf{R}_i(t)$ in the form [29,30]

$$\sigma = \frac{e^2}{6V k_B T} \lim_{t \to \infty} \frac{1}{t} \langle |\mathbf{p}(t)|^2 \rangle, \qquad (14)$$

where the charge moment vector is given by

$$\mathbf{p}(t) \equiv \sum_{i=1}^{N} Q_i [\mathbf{R}_i(t) - \mathbf{R}_i(0)]. \qquad (15)$$

Here, the angular brackets indicate ensemble averaging over initial configurations. In practice, it is expected that only the motions of the Li ions (with charge eQ_{Li}) make significant contributions to the current density, while the current density contributions from the other ions of the system are expected to average to 0. Including only the Li ion contributions to the squared moment vector using Li ion labels ($i = 1, 2, \ldots, M$), we can approximate

$$|\mathbf{p}(t)|^2 \approx Q_{\text{Li}}^2 [\Delta_{\text{self}}(t) + \Delta_{\text{cross}}(t)], \qquad (16)$$

where

$$\Delta_{\text{self}}(t) \equiv \sum_{i=1}^{M} |[\mathbf{R}_i(t) - \mathbf{R}_i(0)]|^2 \qquad (17)$$

and

$$\Delta_{\text{cross}}(t) \equiv \sum_{i=1}^{M} \sum_{j \neq i=1}^{M} [\mathbf{R}_i(t) - \mathbf{R}_i(0)] \cdot [\mathbf{R}_j(t) - \mathbf{R}_j(0)]. \qquad (18)$$

The independent ion contribution $\langle \Delta_{\text{self}}(t) \rangle$ determines the tracer diffusion coefficient D^* according to [29]

$$D^* = \frac{1}{6M} \lim_{t \to \infty} \frac{1}{t} \langle \Delta_{\text{self}}(t) \rangle. \qquad (19)$$

In practice, D^* is estimated from linear fits of computed values of $\Delta_{\text{self}}(t)$ or, equivalently, to the mean-squared displacements (MSD) in the molecular dynamics simulations. The tracer diffusion coefficient D^* can also be measured experimentally [31–33]. In order to relate the Li ion tracer diffusion to the Li ion conductivity, it is convenient to define [29]

$$\sigma = \frac{M}{V} \frac{e^2 Q_{\text{Li}}^2 D^*}{k_B T H_r}. \qquad (20)$$

Here, the Haven ratio (H_r) [31,34] is a measure of the correlation of the conducting ions which also measures the discrepancy between the measured ionic conductivity and the one that would be estimated from the tracer diffusion coefficient used in the Nernst-Einstein relation. If the long time limit of the ensemble average of the ion cross correlation term in the squared charge moment vector $\langle \Delta_{\text{cross}}(t) \rangle$ is zero,

$H_r = 1$. The molecular dynamics runs in this study were analyzed for their tracer diffusion coefficients $D^*(T)$ and using Eq. (20) assuming $H_r = 1$. The results are plotted together with the experimental conductivity in terms of $\log_{10}(T\sigma)$ in Fig. 11. In evaluating Eq. (20), we have assumed that $Q_{\text{Li}} = 1$ which is consistent with the calculated Born effective charge [20] on a Li site.

The comparison in Fig. 11 between the calculated results from calculated tracer diffusion coefficients and the experimental measurements of ionic conductivity suggest that this system has a very large value of the Haven ratio $H_r \gg 1$. As mentioned above, the molecular dynamics simulations may have some statistical errors, particularly at the lower temperatures. However, our analysis suggests that longer simulation times would not change the qualitative evidence for the large Haven ratio. The results also suggest that the Haven ratio is temperature dependent, varying between $H_r(T = 470 \text{ K}) \approx 1 \times 10^2$ and $H_r(T = 310 \text{ K}) \approx 2 \times 10^5$. According to the analysis derived from the Kubo formalism, we see that in order to achieve $H_r > 1$ the long time ensemble average of $\langle \Delta_{\text{cross}}(t) \rangle$ must be less than zero, which can occur when correlated ions hop in opposite directions. Analyzing our molecular dynamics simulations at the lower-temperature runs, we see evidence of $\langle \Delta_{\text{cross}}(t) \rangle < 0$, however, we do not have enough statistics within the current simulations to make a quantitative analysis of this term. It is documented [35] that while the independent ion contribution $\langle \Delta_{\text{self}}(t) \rangle$ is accessible within molecular dynamics simulations, the ion pair correlation contribution $\langle \Delta_{\text{cross}}(t) \rangle$ is very difficult to converge. Typically, Haven ratios for lattice systems are less than 1 [29]. A few recent reports of computed Haven ratios in other electrolytes find $H_r < 1$ [36,37]. On the other hand, there have been a few reports of large Haven ratios for proton diffusion [38] and for simulations of Ag migration in phases of AgI [39]. In both of these cases, correlated motions of the active ion could be proposed. In cubic Li_2OHCl, we expect that the Li ion motions are correlated through their interaction with the neighboring OH orientations. For example, we find that there seems to be a preference for the OH groups to be oriented toward the Li vacancy sites, as discussed further below.

The diffusion coefficient and conductivity are temperature dependent. It is often the case that the tracer diffusion coefficient has an Arrhenius form for the temperature dependence:

$$D^*(T) = D_0^* e^{-E_a/(k_B T)}, \qquad (21)$$

where E_a measures the activation energy for the process. Fitting the simulated tracer diffusion results to Eq. (21), we estimate $E_a^{\text{tracer}} = 0.12 \pm 0.02$ eV. Fitting the measured $\log(T\sigma)$ versus $1/T$ results in the temperature range 330–500 K, we estimate that the corresponding conductivity activation energy for the cubic phase is $E_a^{\sigma} = 0.70 \pm 0.02$ eV. A closer examination of the measured $\log(T\sigma)$ plots shows a small deviation from pure Arrhenius behavior similar to a system reported in the literature which was modeled as having a distribution of activation barriers due to configurational disorder [40]. For cubic Li_2OHCl, due to the disorder in Li ion sites and OH orientations, it seems reasonable that there would be a distribution of local activation barriers for site hopping. The large difference between the calculated E_a^{tracer} and E_a^{σ}
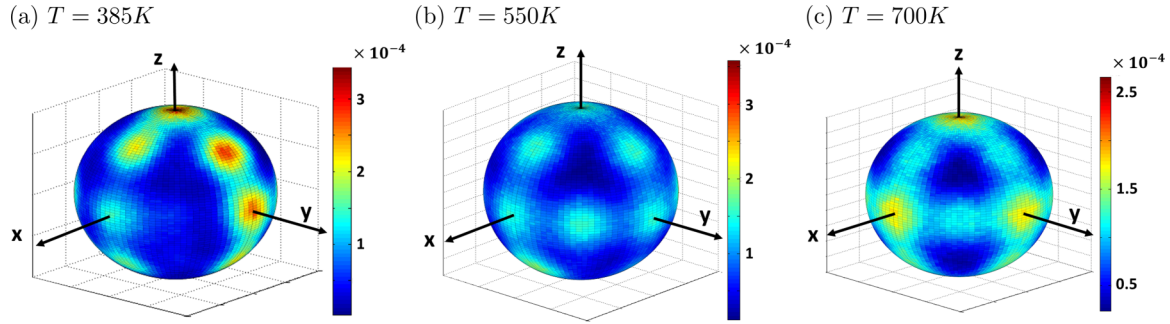
FIG. 12. Plots of the probability densities for OH angles $\mathcal{A}(\theta,\phi)$ at three representative temperatures evaluated from histograms of the molecular dynamics simulations.

implies that the mechanisms involved in the two processes are quite different, as is consistent with the notion that the Li ion motions are correlated during conductivity measurements.

One important characteristic of the cubic structure of Li_2OHCl compared with the orthorhombic phase is the variation in the OH bond directions. Our analysis of the quantum effects of H from the quasiharmonic treatment of lattice vibrations suggests that the rotations of OH bonds may have significant quantum contributions, which is beyond the purview of this study. However, the molecular dynamics simulations do provide a classical treatment of the OH orientations within the various ensembles studied as a function of temperature. For one of the prepared $3 \times 3 \times 3$ supercells of the cubic structure and a set of simulations at three representative temperatures, the atomic configurations at each time step were used to make histograms of the OH bond angles, $\mathcal{A}(\theta,\phi)$, in terms of θ, measured with respect to the lattice **c** axis, and ϕ, measured with respect to the lattice **a** axis. In order to interpret $\mathcal{A}(\theta,\phi)$ as a probability density of finding the OH bonds at each θ and ϕ orientation, it has been normalized over the unit sphere. In Fig. 12, plots of $\mathcal{A}(\theta,\phi)$ are presented, in terms of their projection onto the unit sphere, for simulations at $T = 385$, 550, and 700 K in Figs. 12(a), 12(b), and 12(c), respectively. In principle, these plots should exhibit the cubic symmetry of the system in the ergodic limit of the simulation. For the lowest-temperature simulation of $T = 385$ K, we expect the asymmetry shown in the plot is due to the fact that the system is moving more slowly and sampling fewer configurations. The results for $\mathcal{A}(\theta,\phi)$ evaluated at $T = 385$ and at 550 K suggest that OH bonds are equally likely to be oriented along the $\langle 100 \rangle$ and $\langle 110 \rangle$ directions. At the highest temperature analyzed, the probability density is more diffuse, but suggests that the OH bonds are likely to be concentrated within $\{110\}$ planes; there is a minimum probability of the bond to oriented along the $\langle 111 \rangle$ directions.

Comparing the structural diagrams for the tetragonal and orthorhombic phases (Fig. 1) and the cubic phase (Fig. 8), it is apparent that the orientation of the OH bonds in Li_2OHCl affects the Li ion positions. One way to visualize the motion of the Li ions and the H orientations is to construct a time superposed structural diagram as shown in Fig. 13. These figures were constructed from a molecular dynamics simulation at $T = 640$ K by keeping the Cl and O sites at their initial positions while snapshots of the Li and H positions were superposed for time intervals of 15 fs during 3.5 ps. Figure 13

shows this time superposed diagram from two vantage points: the first in Fig. 13(a) shows the entire simulation cell, and the second in Fig. 13(b) shows the slice made by the black rectangular box in Fig. 13(a) turned about the *a* axis to face the viewer. In both Figs. 13(a) and 13(b), the black oval encloses a lithium hopping event. The hopping event observed is consistent with the direct site hopping mechanism that was proposed by Li, Zhou, *et al.* [2] in their study of similar systems. While in this time superposed diagram, the time sequence of motions is lost, the concentration of hydrogen positions (blue) near the sites corresponding to Li ion vacancies (represented by black boxes) shown in Fig. 13(b) suggests correlation between the two. The time sequence arrows in the diagram also lend further support to the notion that OH orientations act to "gate" the Li ion hops.

In order to get further insight into the Li ion dynamics in the cubic phase of Li_2OHCl, it is convenient to define a quantitative parameter to gain insight into the time dependence of the occupation of the available Li sites. In the structure section, it was shown how the Li site disorder implies the lithiums being randomly distributed in space across the available sites, giving a $\frac{2}{3}$ spatial average of the lithium site occupancy. For each site i, it is convenient to define an average occupancy parameter:

$$\langle S_i(t) \rangle_{time} \equiv \frac{1}{t} \int_0^t S_i(t')dt', \tag{22}$$

where

$$S_i(t) \equiv \begin{cases} 1 & \text{if site } i \text{ is occupied at time } t, \\ 0 & \text{if site } i \text{ is not occupied at time } t. \end{cases} \tag{23}$$

For this purpose, each Li was assigned to the closest lattice site. In time, as the Li ion hops between all sites with equal probability, we expect that the asymptotic value of the average occupancy parameter is

$$\lim_{t \to \infty} (\langle S_i(t) \rangle_{time}) = \frac{2}{3}. \tag{24}$$

In order to monitor the Li ion hopping as a function of time t, it is convenient to define the following ergodicity measure:

$$E_m(t) = \left\langle \left| \frac{2}{3} - \langle S_i(t) \rangle_{time} \right| \right\rangle_{sites}. \tag{25}$$

For our system, initialized with random occupation of the fractionally occupied Li sites, $E_m(t=0) = \frac{4}{9}$. As the sim-
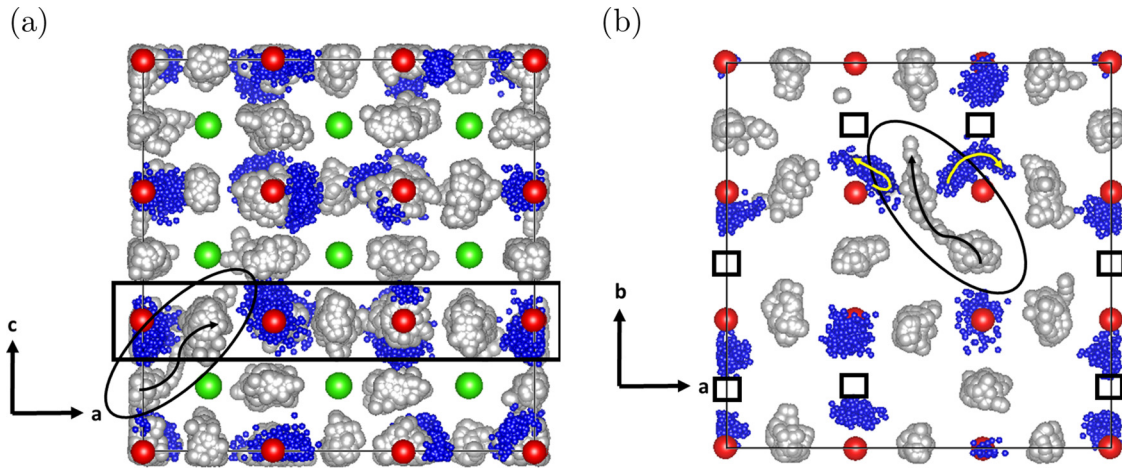
FIG. 13. Time superposed structural diagram of molecular dynamics simulation at $T = 640$ K using the same ball conventions as used in Fig. 8. Cl and O sites are represented at their initial positions and no OH bonds are drawn. Small black boxes indicate Li vacancy positions. Snapshots of the Li and H positions at 15-fs time intervals within the 3.5-ps simulations are superposed in the diagram. A black oval encloses Li site hops which have been completed during the simulation. The curved black arrows indicate the time sequence of the Li motion with the arrow tip corresponding to the latest time. The curved yellow arrows similarly indicate the time sequence of the H motions. (a) Shows the entire simulation cell projected on to the **a-c** plane. (b) Shows a slice of the simulation indicated by the black rectangle in (a), projected onto the **a-b** plane.

ulation proceeds with Li hopping events, we expect that $E_m(t)$ will decrease in time. Because of the asymptotic value of the average occupancy parameter noted in Eq. (24), the asymptotic value of the ergodicity measure must be $E_m(t \rightarrow \infty) = 0$. The behavior of $E_m(t)$ for the molecular dynamics simulations gives information about the Li ion hopping events and a measure of their ergodicity, as illustrated in Fig. 14 for the molecular dynamics simulations with two initial configurations. For our simulations, $E_m(t)$ does decrease with time, but within the simulation times of the current work, the asymptotic limit has not been reached even at the highest simulation temperatures. The values of $E_m(t)$ were averaged over initial times, so that the early times in the plot have better statistics. The results show that the higher-temperature simulations have increased ion hopping as expected, but the lower-temperature simulations need much longer times to achieve equivalent values of $E_m(t)$.

V. SUMMARY AND CONCLUSIONS

In this work, the structural and electrolyte properties of Li_2OHCl are examined. By comparing theoretical results to slow-cooled pristine samples of Li_2OHCl, a reasonable model of the low-temperature orthorhombic structure is found. The quasiharmonic approximation is found to improve the agreement of the simulations with experiment. A theoretical ground-state tetragonal structure is also found that has not been experimentally observed.

Structural calculations of the disordered cubic phase are in good agreement with experiment, particularly for large ($5 \times 5 \times 5$) supercells. Moreover, the comparison of models of the ordered structures to the cubic structure can be described in terms of the availability of new sites for Li ion motion related to the OH bond directions. This is consistent to the abrupt change in ionic conductivity observed at the phase transition. Molecular dynamics simulations of tracer diffusion
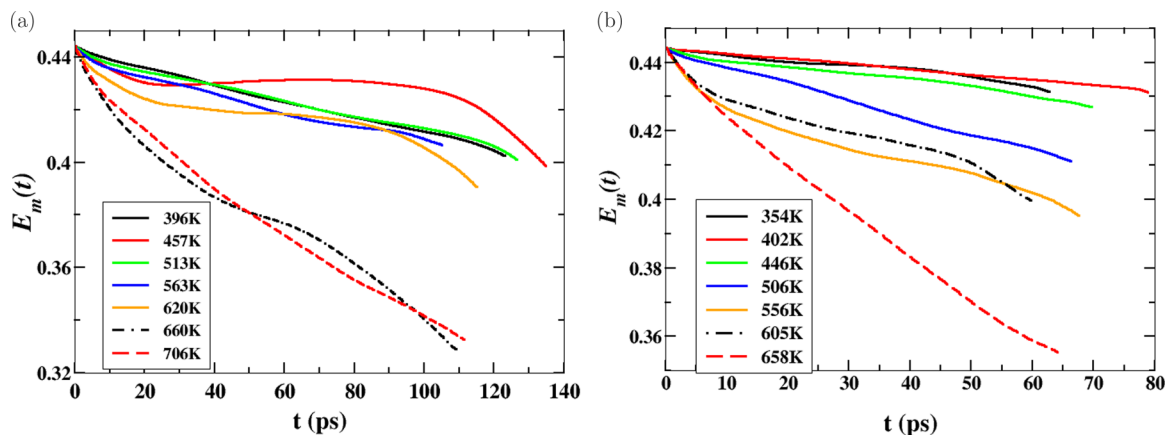

FIG. 14. (a), (b) Show plots of $E_m(t)$ as defined in Eq. (25) for two different initial configurations of cubic Li_2OHCl modeled in $3 \times 3 \times 3$ simulation cells. The legends list the average temperature of each simulation.

in the cubic phase are used to estimate ionic conductivity assuming no correlations among the mobile ion motions. The results show a large discrepancy with the experimental ionic conductivity measurement. The discrepancy gives evidence of a large temperature-dependent Haven ratio, indicating highly correlated Li ion motion. Molecular dynamics simulations also give evidence of a relationship between the OH orientations toward vacant Li sites. The OH bond orientations are suggested to participate in a gating mechanism for Li ion conduction. For analyzing the results, an ergodicity measure has been defined which goes to zero when all of the available Li sites have achieved their average occupation.

The combined experimental and computational study of well-formed Li_2OHCl structures should help inform the further development of this material as an electrolyte for all solid-state Li ion batteries as discussed in the recent literature [1,2].

[1] Z. D. Hood, H. Wang, A. Samuthira Pandian, J. K. Keum, and C. Liang, J. Am. Chem. Soc. **138**, 1768 (2016).

[2] Y. Li, W. Zhou, S. Xin, S. Li, J. Zhu, X. Lü, Z. Cui, Q. Jia, J. Zhou, Y. Zhao, and J. B. Goodenough, Angew. Chem., Int. Ed. **55**, 9965 (2016).

[3] C. Eilbracht, W. Kockelmann, D. Hohlwein, and H. Jacobs, Phys. B (Amsterdam) **234**, 48 (1997).

[4] G. Schwering, A. Hönnerscheid, L. van Wüllen, and M. Jansen, Chem. Phys. Chem. **4**, 343 (2003).

[5] P. Hartwig, A. Rabenau, and W. Weppner, J. Less-Common Met. **78**, 227 (1981).

[6] P. Hohenberg and W. Kohn, Phys. Rev. **136**, B864 (1964).

[7] W. Kohn and L. J. Sham, Phys. Rev. **140**, A1133 (1965).

[8] P. E. Blöchl, Phys. Rev. B **50**, 17953 (1994).

[9] N. A. W. Holzwarth, A. R. Tackett, and G. E. Matthews, Comput. Phys. Commun. **135**, 329 (2001), available from the website http://pwpaw.wfu.edu.

[10] P. Giannozzi, S. Baroni, N. Bonini, M. Calandra, R. Car, C. Cavazzoni, D. Ceresoli, G. L. Chiarotti, M. Cococcioni *et al.*, J. Phys.: Condens. Matter **21**, 395502 (2009), available from the website http://www.quantum-espresso.org.

[11] K. Momma and F. Izumi, Appl. Crystallogr. **44**, 1272 (2011), code available from the website http://jp-minerals.org/vesta/en/.

[12] A. Kokalj, J. Mol. Graphics Modell. **17**, 176 (1999), code available at the website http://www.xcrysden.org.

[13] H. T. Stokes and D. M. Hatch, J. Appl. Crystallogr. **38**, 237 (2008), available from the webpage http://iso.byu.edu/iso/isotropy.php.

[14] MATLAB, The MathWorks, Inc., Natick, Massachusetts, United States.

[15] J. P. Perdew and Y. Wang, Phys. Rev. B **45**, 13244 (1992).

[16] Y. A. Du and N. A. W. Holzwarth, Phys. Rev. B **76**, 174302 (2007).

[17] Y. A. Du and N. A. W. Holzwarth, Phys. Rev. B **81**, 184106 (2010).

[18] Z. D. Hood, C. Kates, M. Kirkham, S. Adhikari, C. Liang, and N. A. W. Holzwarth, Solid State Ionics **284**, 61 (2015).

[19] X. Gonze and J.-P. Vigneron, Phys. Rev. B **39**, 13120 (1989).

[20] P. Giannozzi, S. de Gironcoli, P. Pavone, and S. Baroni, Phys. Rev. B **43**, 7231 (1991).

[21] S. Baroni, S. de Gironcoli, A. Dal Corso, and P. Giannozzi, Rev. Mod. Phys. **73**, 515 (2001).

[22] *International Tables for Crystallography, Volume A: Space-Group Symmetry, Fifth Revised Edition*, edited by T. Hahn (Kluwer, Dordrecht, 2002). The symmetry labels used in this work are all based on this reference.

[23] K. Azuma, T. Oda, and S. Tanaka, Comput. Theor. Chem. **963**, 215 (2011).

[24] A. Maradudin, *Theory of Lattice Dynamics in the Harmonic Approximation, Second Edition*, Solid State Physics: Supplement, Vol. 3 (Academic, New York, 1971).

[25] M. Born and K. Huang, *Dynamical Theory of Crystal Lattices* (Oxford University Press, Oxford, 1954).

[26] S. Baroni, P. Giannozzi, and E. Isaev, Rev. Mineral. Geochem. **71**, 39 (2010).

[27] C. Lee and X. Gonze, Phys. Rev. B **51**, 8610 (1995).

[28] R. Kubo, J. Phys. Soc. Jpn. **12**, 570 (1957).

[29] G. Murch, Solid State Ionics **7**, 177 (1982).

[30] J. M. Haile, *Molecular Dynamics Simulation: Elementary Methods* (Wiley, New York, 1992).

[31] Y. Haven and B. Verkerk, Physics and Chemistry of Glasses **6**, 38 (1965).

[32] S. Takai, K. Yoshioka, H. Iikura, M. Matsubayashi, T. Yao, and T. Esaka, Solid State Ionics **256**, 93 (2014).

[33] N. Kuwata, X. Lu, T. Miyazaki, Y. Iwai, T. Tanabe, and J. Kawamura, Solid State Ionics **294**, 59 (2016).

[34] K. Campaan and Y. Haven, Trans. Faraday Soc. **54**, 1498 (1958).

[35] M. J. Castiglione and P. A. Madden, J. Phys.: Condens. Matter **13**, 9963 (2001).

[36] A. Marcolongo and N. Marzari, Phys. Rev. Mater. **1**, 025402 (2017).

[37] X. He, Y. Zhu, and Y. Mo, Nat. Commun. **8**, 15893 (2017).

[38] M. Spaeth, K. Kreuer, J. Maier, and C. Cramer, J. Solid State Chem. **148**, 169 (1999).

[39] B. J. Morgan and P. A. Madden, Phys. Rev. Lett. **112**, 145901 (2014).

[40] C. Bischoff, K. Schuller, S. P. Beckman, and S. W. Martin, Phys. Rev. Lett. **109**, 075901 (2012).